Seasonal and dust-related variations in the dayside thermospheric and ionospheric compositions of Mars observed by MAVEN/NGIMS

Nao Yoshida, Naoki Terada, Hiromu Nakagawa, David A. Brain, Shotaro Sakai, Yuki Nakamura, Mehdi Benna, Kei Masunaga

JGR Planets

RESEARCH ARTICLE
10.1029/2021JE006926

Key Points:

- Seasonal variations in CO_2^+ and O_2^+ in the ionosphere are significant, while those in O^+ are less discernible
- The observed variations in CO_2^+ and O^+ are well reproduced by a photochemical equilibrium model
- Decreases in O, O^+, and O_2^+ densities in the thermosphere and ionosphere are found during a regional dust storm

Correspondence to:
N. Yoshida,
nao.yoshida.q7@dc.tohoku.ac.jp

Citation:
Yoshida, N., Terada, N., Nakagawa, H., Brain, D. A., Sakai, S., Nakamura, Y., et al. (2021). Seasonal and dust-related variations in the dayside thermospheric and ionospheric compositions of Mars observed by MAVEN/NGIMS. *Journal of Geophysical Research: Planets*, *126*, e2021JE006926. https://doi.org/10.1029/2021JE006926

Received 13 APR 2021
Accepted 26 OCT 2021

Author Contributions:
Conceptualization: Nao Yoshida, David A. Brain
Formal analysis: Nao Yoshida
Funding acquisition: Nao Yoshida, Naoki Terada, Hiromu Nakagawa
Investigation: Nao Yoshida
Resources: Shotaro Sakai, Yuki Nakamura, Mehdi Benna
Supervision: Naoki Terada, Hiromu Nakagawa
Visualization: Nao Yoshida
Writing – original draft: Nao Yoshida
Writing – review & editing: Nao Yoshida, Naoki Terada, Hiromu Nakagawa, David A. Brain, Shotaro Sakai, Mehdi Benna, Kei Masunaga

Seasonal and Dust-Related Variations in the Dayside Thermospheric and Ionospheric Compositions of Mars Observed by MAVEN/NGIMS

Nao Yoshida[1], Naoki Terada[1], Hiromu Nakagawa[1], David A. Brain[2], Shotaro Sakai[1,3], Yuki Nakamura[1,4], Mehdi Benna[5], and Kei Masunaga[2,6]

[1]Graduate School of Science, Tohoku University, Sendai, Japan, [2]Laboratory for Atmospheric and Space Physics, University of Colorado, Boulder, CO, USA, [3]Graduate School of Science, Planetary Plasma and Atmospheric Research Center, Tohoku University, Sendai, Japan, [4]LATMOS/CNRS, Sorbonne Université, Paris, France, [5]University of Maryland, Baltimore, MD, USA, [6]Institute of Space and Astronautical Science, Japan Aerospace Exploration Agency, Chōfu, Japan

Abstract We report seasonal and dust-related variations in neutral and ion species (CO_2, O, and N_2, and CO_2^+, O_2^+, O^+, and N^+, respectively) in the dayside Martian upper atmosphere between altitudes of ~150 and ~250 km observed by the Neutral Gas and Ion Mass Spectrometer aboard the Mars Atmosphere and Volatile Evolution spacecraft. The sinusoidal seasonal variations in CO_2^+ and O_2^+ densities are clearly identified, while that of O^+ is less discernible. These observed variations in ion densities are well reproduced by a photochemical equilibrium model for CO_2^+ and O^+ densities when we combine them with solar cycle variations. Furthermore, we find a decrease in O, O^+, and O_2^+ densities in the whole altitude range at L_s = 342–346 in MY 33 during a regional dust event. The decrease in O density would lead to decreases in O^+ and O_2^+ densities in the ionosphere through ion-neutral reactions. Observed variations in ion and neutral species associated with the season and a regional dust storm are also confirmed in pressure coordinates. Observations show that the CO_2^+/O^+ ratio at a given pressure level in the ionosphere varies by a factor of ~3, which can modify the composition of ion outflow from the Martian atmosphere.

Plain Language Summary Early Mars had a dense CO_2 atmosphere that could sustain a significant amount of liquid water, but present Mars only has a 7–9 mbar CO_2 atmosphere. Many CO_2 gases are considered to have been lost to space. One of the mechanisms for atmospheric escape on Mars is the acceleration of the ion species in the ionosphere by the interaction with the solar wind. Since ionospheric ions can be the source of escaping ions, variability in the number density in the ionosphere might affect the escape rates. The Neutral and Gas and Ion Mass Spectrometer aboard the Mars Atmosphere and Volatile Evolution spacecraft can provide a long-term data set of number densities and composition in the ionosphere and thermosphere. We investigated the compositional change in number densities in the ionosphere and thermosphere because they are coupled through ion-neutral reactions. Seasonal variations in neutral and ion densities are observed, and we find that the number densities of O, O^+, and O_2^+ decrease when a regional dust storm occurs in the lower atmosphere.

1. Introduction

The Martian upper atmosphere is the reservoir region for an atmospheric escape to space. The escape rates of O_2^+, O^+, and CO_2^+ ions of Martian origin and their relative ratios have been measured by ion mass spectrometers aboard Mars Express (e.g., Carlsson et al., 2006; Lundin et al., 2009) and Mars Atmosphere and Volatile Evolution (MAVEN; e.g., Inui et al., 2018, 2019). The source altitude of ion outflow is located below ~250 km since the composition of ion, the outflow is similar to that of the ionosphere below ~250 km as measured by the Viking-1 probe (Lundin et al., 2004, 2007). It is well known that the escape rates of planetary ions from Mars change in response to the solar wind and solar extreme ultraviolet (EUV) fluxes (e.g., Dong et al., 2017; Dubinin, Fraenz, Pätzold, Andrews, et al., 2017; Lundin et al., 2008). A multifluid magnetohydrodynamic model in C. Dong et al. (2015) suggested that the ion escape rate varies seasonally by a factor of ~1.3, where it is enhanced at perihelion but depleted at aphelion. However, the seasonal variation

in the composition of the reservoir region, that is, the thermosphere and ionosphere, and its connection to the composition of escaping ions are open questions due to the lack of long-term continuous observations of thermospheric and ionospheric compositions on Mars.

The composition of the ionosphere in the photochemical equilibrium (PCE) layer below an altitude of ~200 km on Mars (e.g., Fox et al., 2017) is tightly coupled with the thermospheric composition through ion-neutral reactions. In the PCE layer where the time scale for photochemical loss is shorter than that for transport, the number densities of ion species are derived under the assumption that the production and loss rates of ions are equal. Important photochemical production and loss processes for the major ionospheric ions, O_2^+, O^+, and CO_2^+, are

$$CO_2 + hv \rightarrow CO_2^+ + e \quad (1)$$

$$O + hv \rightarrow O^+ + e \quad (2)$$

$$CO_2 + hv \rightarrow O^+ + CO + e \quad (3)$$

$$O + CO_2^+ \rightarrow CO_2 + O^+, \quad k_1 = 9.6 \times 10^{-11} \left[\mathrm{cm^3 s^{-1}}\right] \quad (4)$$

$$O^+ + CO_2 \rightarrow CO + O_2^+, \quad k_2 = 1.1 \times 10^{-9} \left[\mathrm{cm^3 s^{-1}}\right] \quad (5)$$

$$O + CO_2^+ \rightarrow CO + O_2^+, \quad k_3 = 1.6 \times 10^{-10} \left[\mathrm{cm^3 s^{-1}}\right] \quad (6)$$

$$O_2^+ + e \rightarrow O + O, \quad k_4 = 2.4 \times 10^{-7} \left(300 / Te\right)^{0.7} \left[\mathrm{cm^3 s^{-1}}\right] \quad (7)$$

$$CO_2^+ + e \rightarrow CO + O, \quad k_5 = 4.2 \times 10^{-7} \left(300 / Te\right)^{0.75} \left[\mathrm{cm^3 s^{-1}}\right] \quad (8)$$

where the reaction rate coefficients are taken from Schunk and Nagy (2009).

According to PCE theory, the number densities of the major ions strongly depend on thermospheric CO_2 and O number densities, which are mainly controlled by thermospheric temperature (i.e., scale heights), and dissociation by far-ultraviolet (FUV) radiation. The variations and structures of ion densities with solar activity have been simulated in previous models (e.g., Bougher et al., 2015; Fox et al., 1996; Krasnopolsky, 2002). Seasonal variations in thermospheric temperature correlate with solar EUV irradiance (Bougher et al., 2017; Thiemann et al., 2018). It is noted that the distribution of the O number density is mainly controlled by global wind advection and diffusion above an ~170 km altitude due to its small atomic mass (Bougher et al., 1990, 1999). Thermospheric general circulation models have shown that the O density is depleted around the afternoon and enhanced around midnight owing to transport by global wind (Bougher et al., 1990, 2015).

Recently, the homopause of Mars was observed to vary between altitudes of 60 and 140 km (Jakosky et al., 2017; Slipski et al., 2018). Additionally, seasonal variations in the N_2/CO_2 ratio at an altitude of 140 km in the lower thermosphere were investigated by the Imaging UltraViolet Spectrograph (IUVS) aboard MAVEN (Yoshida et al., 2020). The N_2/CO_2 ratio at 140 km showed a maximum near aphelion and a minimum near perihelion and varied by a factor of two. It was concluded that the variations in the N_2/CO_2 ratio are mainly controlled by the change in the homopause altitude. Yoshida et al. (2020) also suggested that the dayside homopause altitude would be mainly controlled by the inflation and contraction of the lower atmosphere. The variations in the homopause altitude and the atmospheric composition at a constant altitude in the lower thermosphere suggest that the neutral and ion compositions in the upper atmosphere would change seasonally, responding to the lower atmospheric variations. The seasonal variation in the ion composition related to that of the homopause altitude was predicted by a general circulation model (GCM) (Chaufray et al., 2014). They suggested that the average dayside density ratios of CO_2^+/O^+ and O_2^+/O^+ can be enhanced by up to one order of magnitude at a pressure level of 8×10^{-8} Pa in the solstice season, when the homopause altitude and its pressure level are high and low, respectively. However, observational validation has not been conducted. The upper atmospheric density is enhanced during both global and regional dust

events due to the heating and expansion of the lower atmosphere (e.g., Keating et al., 1998; Liu et al., 2018; Withers & Pratt, 2013). Fang et al. (2020) suggested that ionospheric compositional change is significant during a global dust event but is less remarkable during a regional dust event. They also mentioned that a significant change in ionospheric composition during a global dust event leads to an enhancement of the CO_2^+ escape rate. Unexpected decreases in O during a global dust storm event were found in observations of the thermosphere (Elrod et al., 2019). The ionospheric compositions were also modified according to the atmospheric composition in the neutral atmosphere (Niu et al., 2021), which might support the idea that the escape of major ions would be modified by a global dust event. However, it is not clear how the composition in the upper atmosphere changes during a regional dust event. The transport of water vapor from the lower atmosphere has been observed during such events (Aoki et al., 2019; Fedorova et al., 2018; Heavens et al., 2018). An enhancement of H_2O ions was observed in the ionosphere during both regional and global dust storms (Stone et al., 2020). These facts suggest that the upper atmospheric composition may change during a regional dust event.

The Neutral Gas and Ion Mass Spectrometer (NGIMS) aboard MAVEN measures both neutral and ion densities in the range of ~150–500 km altitudes (Mahaffy et al., 2015). Using NGIMS observations, a strong connection between the thermosphere and ionosphere was reported (Withers et al., 2015). Girazian et al. (2019) investigated that seasonal, solar zenith angle (SZA), and solar flux variations in the O^+ peak density and concluded that the O^+ peak density is mainly controlled by the O/CO_2 ratio at the same altitude as predicted by photochemical theory. Above the O^+ peak, the O^+/O_2^+ ratio in the dayside is 1.1 ± 0.6 and decreases with increasing SZA (Girazian et al., 2019). The investigation of vertical profiles of CO_2^+, O_2^+, and O^+ in the ionosphere can be used to estimate the source altitude of ion outflow (cf. Lundin et al., 2004, 2007). Furthermore, clarifying the variability in these ion species is important to understand the connection between the ionosphere and ion outflow.

In this study, we investigate the seasonal variations in neutral and ion compositions in the upper atmosphere (thermosphere and ionosphere) as well as their response to a regional dust storm. The purposes of this paper are (a) to confirm the vertical coupling between the lower thermosphere and the upper thermosphere and (b) to verify the coupling between the thermosphere and the ionosphere in the dayside between altitudes of ~150 and 250 km over a Mars season. We discuss whether heavy ion outflow can be affected by seasonal variations in the upper atmospheric composition. In-situ observations of N_2 and CO_2 density profiles by NGIMS are examined and compared to previous IUVS observations of the N_2/CO_2 seasonal variation in the lower thermosphere (Yoshida et al., 2020). To understand the second purpose and discuss the effects on the composition of heavy ion outflows, we examine O, CO_2, O^+, O_2^+, and CO_2^+ density profiles.

The data set we used in this study is presented in the next section. The time variations and vertical structures of the neutral and ion densities are shown in Section 3. We discuss the seasonal variation in ion densities under the PCE in Section 4. We also describe the variation in ionospheric compositions when a regional dust storm occurred in the lower atmosphere in the same section. The effects on the composition of heavy ion outflows are discussed in Section 5. Finally, our conclusions are summarized in Section 6.

2. Instrument and Data Set

NGIMS is a mass spectrometer (Mahaffy et al., 2014) that provides neutral gas and ambient ion compositions. NGIMS can detect species with a range of 2–150 Daltons and a unit mass resolution. In our analysis, we use the upper atmospheric neutral densities of CO_2, N_2, and O as well as ion densities of CO_2^+, N^+, O_2^+, and O^+. It is noted that the abundances of O are derived indirectly by measuring O_2 because atmospheric O interacts with the instrument's walls and forms O_2, which assumes that the number density of O_2 in the thermosphere is negligible compared to that produced in the instrument (Stone et al., 2018). N_2 is selected to confirm the vertical coupling between N_2/CO_2 in the lower thermosphere (Yoshida et al., 2020) and in the upper thermosphere. To investigate the ion-neutral coupling of N_2 in the thermosphere, N^+ is selected. NGIMS measures these densities between an ~500 km altitude and periapsis altitude (normally ~150 km) with a vertical resolution of less than one half scale height for each species. It is noted that the MAVEN spacecraft moves horizontally ~2700 km during a single orbit below 250 km. Thus, a typical single pass spans ~45° of latitude, a few hours of local time, and ~40° of SZA as shown in Figures 1a–1c. Neutral

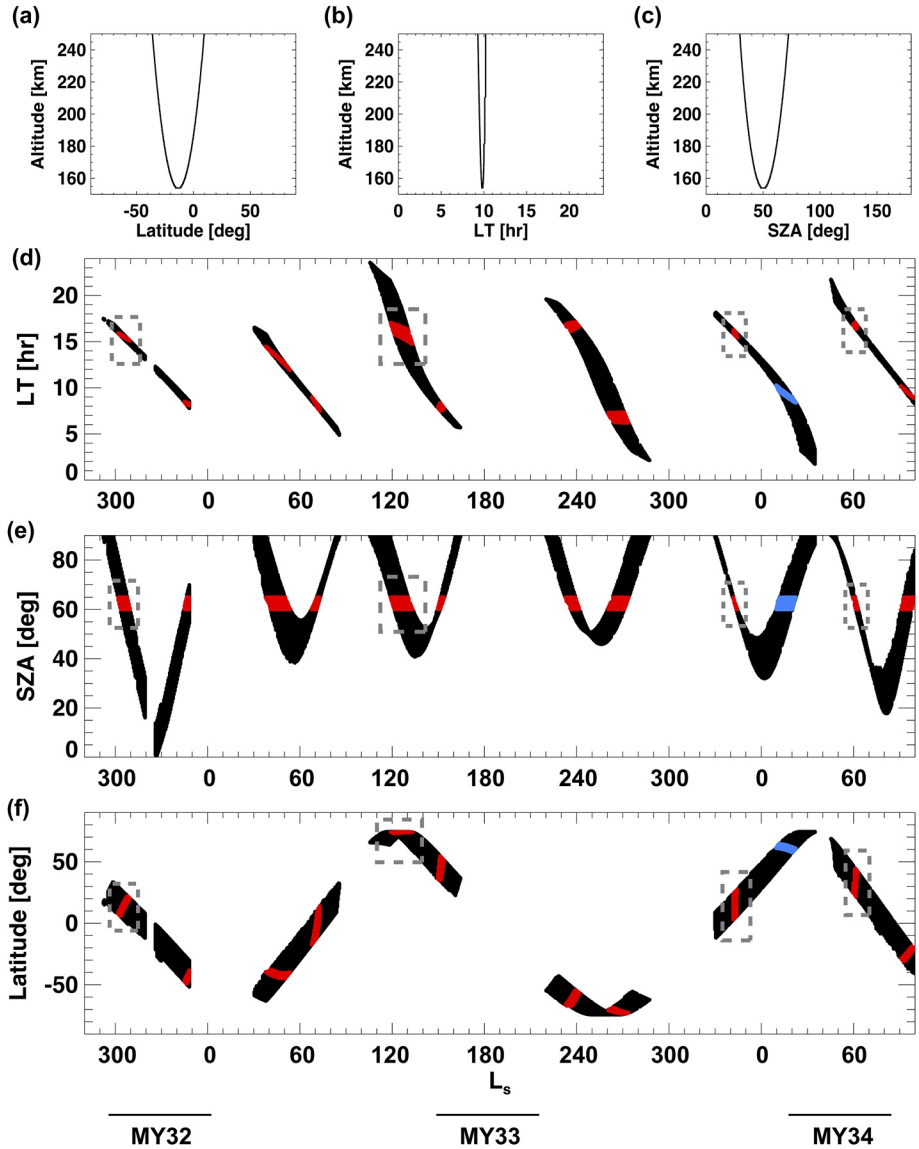

Figure 1. An example of the observing geometry of neutral gas and ion mass spectrometer (NGIMS) observations for orbit number 6163 is shown in (a)–(c). Footprints of NGIMS inbound segment observations where solar zenith angle (SZA) is less than 90° and altitude is less than 250 km are shown in (d) local time (hours), (e) SZA (degree), and (f) latitude (degree). Footprints observed from 60° to 65° in SZA are colored. Red is used for the analysis of both neutral and ion species. Light blue is used for neutral species because ion species are highly affected by spacecraft potential effects. Dashed boxes in panel (d)–(f) indicate the data set used in Figures 4, 5, 9 and 10.

species are measured every orbit, while ion species are obtained every two orbits. The standard deviation in individual ion measurements due to random uncertainties depends on the density and is typical ~50% at 0.1 cm^{-3} and ~25% above 1 cm^{-3} (Benna et al., 2015). The absolute uncertainty of neutral species, such as CO_2 and N_2, is estimated to be less than 20% (Mahaffy et al., 2015). The absolute uncertainty of O density is approximately 25%. It is noted that the background level of reactive species such as CO_2 increases in the outbound segments due to an interaction with the instrument's wall (Mahaffy et al., 2015). Therefore, the data set we applied in this study is restricted to the inbound segments for all species for more precise measurement accuracy.

We used Level 2 version 8 revision 1 of the NGIMS data set provided in the Planetary Data System (PDS) and analyzed the densities of ion and neutral species from February 3, 2015 to December 20–31, 2017. The total number of orbits during that duration reaches 4,478 for neutral species and 2,418 for ion species. The

total duration corresponds to Martian Year (MY) 32 solar longitude (L_s) = 284 to MY 34 L_s = 108. The time evolution of the NGIMS geometry used for our analysis is shown in Figures 1d–1f. To obtain the variation in the dayside, the coverage is limited to less than 90° in SZA. Hereafter, we show the averaged profile observed between 60° and 65° in SZA to restrict the dependences of number density on SZA (e.g., Withers, 2009) because those SZA ranges are included in several L_s ranges and the transport of gas species to the nightside is less effective than around the terminator. The selected data set we used for profile analyses in Section 3 is shown in red in Figures 1d–1f. The data set of ion species are filtered according to the spacecraft potential to be more than −3 V. The ion data observed around L_s ~15 in MY 34, which are colored in light blue in Figures 1d–1f, are removed because the spacecraft potential is less than −6 V and affects the ion density. The data set is measured both in the morning and afternoon as well as in both the northern and southern hemispheres.

The electron temperature profiles observed by the Langmuir Probe and Waves instrument (LPW; Andersson et al., 2015) are used to discuss seasonal variations in ion density under the PCE model in Section 4.1. The local electron temperature is measured in Langmuir Probe (LP) mode, which measures current-voltage characteristics (Andersson et al., 2015; Ergun et al., 2015). The LPW has two independent cylindrical probes. Below an altitude of 500 km, where cold electrons are dominant, the LP instrument operates in a sweeping range from −5 to 5 V, typically with 128 steps, a sweep duration of 1–4 s, and at a cadence of 1–2 sweeps per 4 s. The derived electron temperature is combined from the two probes. We used Level 2 version 3 of the LPW data set provided in the PDS and analyzed the electron temperature profile with the same criteria for geometry as the NGIMS observations. The LPW data contain the quality flags, which represent the confidence of the data set. In this study, we limited the data to those with quality flags greater than 50.

3. Result

3.1. Time Variations in Neutral and Ion Densities at an Altitude of 200 km

Time variations in neutral densities versus L_s in MY 32 to MY 34 are shown in Figure 2. The densities and mixing ratio are shown at a representative altitude of 200 km, which is higher than the typical exobase altitude (Jakosky et al., 2017). The time variation in the orbit-averaged solar EUV irradiance at 17–22 nm observed by the Extreme UltraViolet Monitor (EUVM) aboard MAVEN (Eparvier et al., 2015) is also shown. During the observation time, the solar activity changed gradually from the mean to the minimum. The effects of change of heliocentric distance are also seen in the EUV irradiance. Although L_s ~ 300 in MY 32 is observed when the EUV irradiance is high compared to the other seasons, seasonal variations in CO_2, N_2, and O number densities are obvious. The green dashed line shown in Figures 2b–2d are sinusoidal fitting to the number density observed in the afternoon (light green dots). Note that we excluded the observation at L_s ~ 340 from the fit because it was in a regional dust event. Variation during the regional dust storm is explained in Section 4.2. The seasonal variation is quantified as a function of

$$d = 10^{\left[A \sin\left(L_s - B\right) + C\right]}, \tag{9}$$

where d is the number density at 200 km, A is the amplitude of the seasonal variation, B is the phase, and C is the constant. Higher number densities appear around perihelion (L_s = 251), and lower number densities appear around aphelion (L_s = 71). Variations in the number densities of CO_2, N_2, and O at 200 km in the afternoon are factors of ~9, ~3, and ~4, respectively, based on the median densities between MY 33 L_s ~ 50 and MY 33 L_s ~ 240. The observed sinusoidal seasonal trend of CO_2 at a constant altitude of 200 km has good agreement with previous observations of CO_2 in the thermosphere and mesosphere (Gröller et al., 2018; Forget et al., 2009; Slipski et al., 2018; Yoshida et al., 2020). The variation in CO_2 density is also larger than that in N_2 density at 140 km altitude (Yoshida et al., 2020). These facts suggest that the variation in densities in the upper thermosphere is associated with that in the lower thermosphere and mesosphere. The CO_2 density observed in the morning does not correspond with the sinusoidal curve shown in Figure 2b. This may be the result of diurnal variation (Gupta et al., 2019).

It is noteworthy that the O density at L_s ~ 340 in MY 33 decreases significantly from the sinusoidal fitting. A regional dust event was observed during this period (Montabone et al., 2015, 2020). A decrease in O density

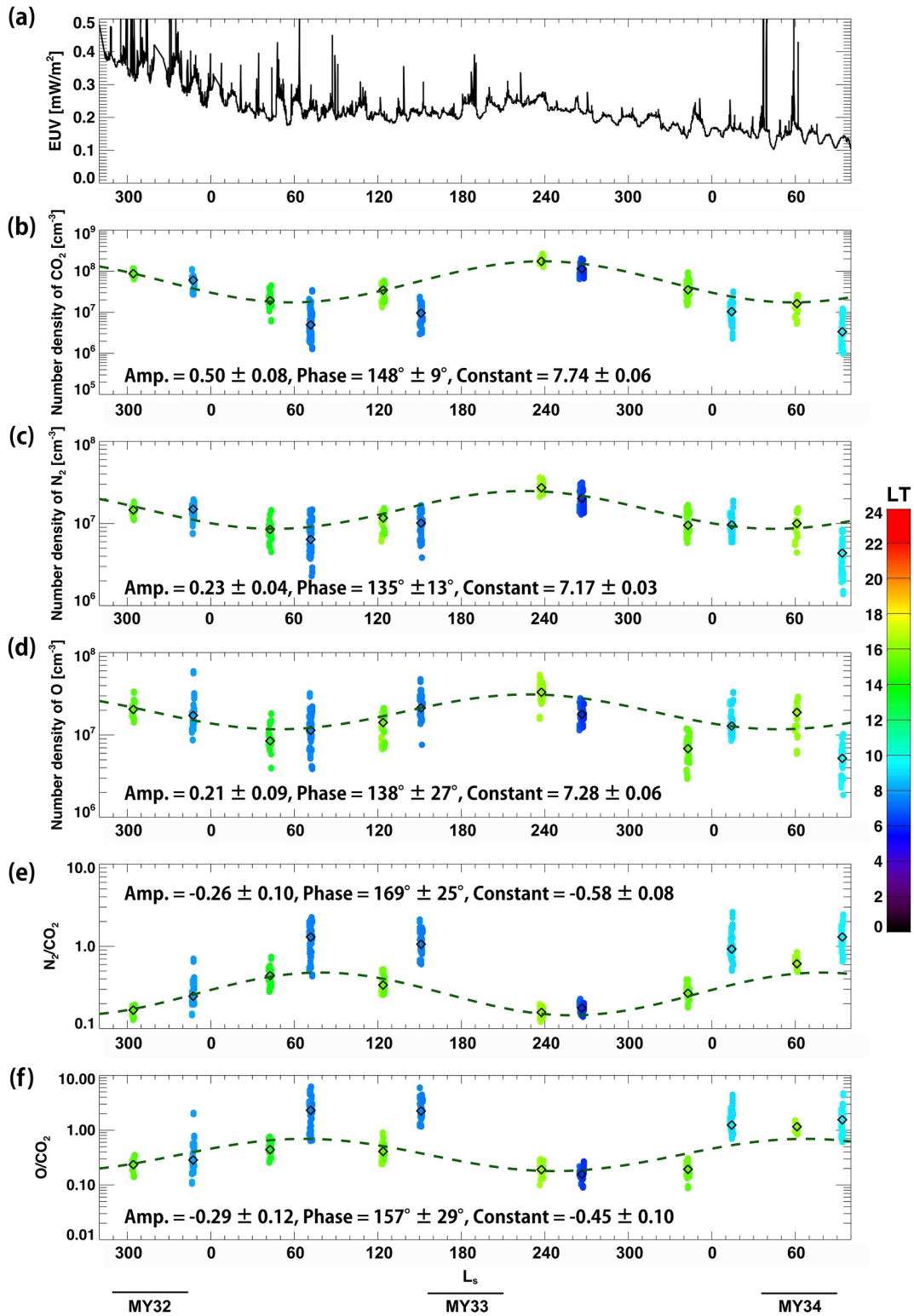

Figure 2. Time variations in (a) Extreme ultra violet irradiance at 17–22 nm, neutral species and their relative abundances observed at 200 km including (b) CO_2, (c) N_2, and (d) O number densities, and (e) N_2/CO_2 and (f) O/CO_2 ratios. The color bar represents the observed local time. Black diamonds indicate the median value of each observational group. The green dashed line shown in (b)–(f) is a sinusoidal fitting to the number density and mixing ratio observed at 200 km only in the afternoon and excludes the data at $L_s \sim 340$ in MY 33 (dust storm data) to show the seasonal variation. The best fit parameters (amplitude, phase, and constant) of sinusoidal fit are shown in the figures.

in the thermosphere during the planet-encircling dust event in 2018 was observed by Elrod et al. (2019) and Niu et al. (2021). We focus on the atmospheric composition during the regional dust event in Section 4.2.

In Figures 2e and 2f, sinusoidal seasonal trends are also visible in the density ratios of N_2/CO_2 and O/CO_2. A sinusoidal fitting corresponding to mixing ratios observed in the afternoon, excluding the regional dust event at $L_s \sim 340$ in MY 33, is shown by the green dashed line in Figures 2e and 2f. N_2/CO_2 varies from 0.15 ($L_s \sim 240$ in MY 33) to 0.44 ($L_s \sim 50$ in MY 33) by a factor of 3. O/CO_2 varies from 0.19 to 0.44 by a factor of 2. The mixing ratio of N_2/CO_2 at a 200 km altitude is higher than that at 140 km observed by IUVS (Yoshida et al., 2020). A higher mixing ratio of lighter species at a 200 km altitude is reasonable due to the diffusive separation in this region. Mixing ratios around the morning terminator show higher values than in the afternoon, which has already been confirmed in previous observations at an altitude of 140 km by IUVS (Yoshida et al., 2020).

Time variations in ion densities versus L_s are shown in Figure 3. CO_2^+, N^+, O_2^+, and O^+ densities at a representative altitude of 200 km are shown. Sinusoidal curves are also fitted as in Figure 2. The seasonal variation in CO_2^+ density resembles that of CO_2 density in Figure 2b. Observations in the afternoon show that the highest CO_2^+ density is 2.6×10^3 cm^{-3} at MY 32 $L_s \sim 300$ and the lowest CO_2^+ density is 3.4×10^2 cm^{-3} at MY 34 $L_s \sim 60$. The CO_2^+ densities measured around the morning show relatively low densities than those around the afternoon; for example, profiles observed at MY 33 $L_s \sim 120$ (at approximately 16:00) and at MY 33 $L_s \sim 160$ (at approximately 8:00), correspond to the dawn-dusk asymmetry of neutral CO_2 densities in Figure 2b. This might be related to the dawn-dusk asymmetry of ion density shown by Benna et al. (2015) and Cui et al. (2020). The N^+ density has an opposite seasonal variation to the CO_2^+ density. The lowest density, 2.2 cm^{-3}, appears at MY 33 $L_s \sim 240$, and the highest density, 6.7 cm^{-3}, appears at MY 34 $L_s \sim 60$. The opposite seasonal variation between CO_2^+ and N^+ densities can be explained by the fact that N^+ is destroyed by photochemical reactions with CO_2. N^+ is produced mainly by photodissociative ionization of N_2, whose production frequency at the optically thin layer is 1.7×10^{-8} s^{-1} at a low solar activity (Fox et al., 1996). N^+ is destroyed by reaction with CO_2 below its peak altitude following the reactions (Fox & Sung, 2001)

$$N^+ + CO_2 \rightarrow CO^+ + NO, \quad k = 2.02 \times 10^{-10} \left[\text{cm}^3\text{s}^{-1}\right] \tag{10}$$

$$N^+ + CO_2 \rightarrow N + CO_2^+, \quad k = 9.18 \times 10^{-10} \left[\text{cm}^3\text{s}^{-1}\right] \tag{11}$$

Figure 2 shows that the variations in CO_2 density have a larger amplitude than the variations in N_2 density, which would enhance the loss process for N^+. The production rate of N^+ would not change seasonally because the seasonal variation in N_2 density is approximately one-third of the CO_2 density at a 200 km altitude. Thus, the net N^+ density should decrease according to an increase in the CO_2 density. Consequently, we confirmed that seasonal variations in number densities in the upper thermosphere corresponding to those in the lower thermosphere lead to variations in N^+ and CO_2^+ densities at 200 km. The O_2^+ density also shows a seasonal variation similar to the CO_2^+ density. A seasonal variation in O^+ density is less discernible. We focus on these aspects in the next section.

3.2. Vertical Structures of Neutral and Ion Densities

Median vertical profiles of neutral densities are investigated in the altitude range of ~150–240 km, which are shown in Figure 4. To examine the coupling between the ionosphere and thermosphere, we selected data obtained in the northern hemisphere, SZA between 60° and 65°, and local time later than 12:00 p.m., whose data are indicated by the dashed boxes in Figures 1d–1f. Local time is constrained in the afternoon because of the asymmetry of the density between day and night (Benna et al., 2015; Cui et al., 2020; Gupta et al., 2019). The profiles observed in the northern hemisphere are particularly suitable for understanding ion-neutral photochemical coupling because the ionospheric density is enhanced due to the strong crustal magnetic field in the southern hemisphere (Withers et al., 2019).

Vertical profiles are shown for specific L_s bins, including L_s = 59–63 in MY 34, L_s = 113–133 in MY 33, L_s = 299–310 in MY 32, and L_s = 342–346 in MY 33, which correspond to the northern hemisphere late spring, summer, winter, and late winter, respectively. A profile including the regional dust storm event

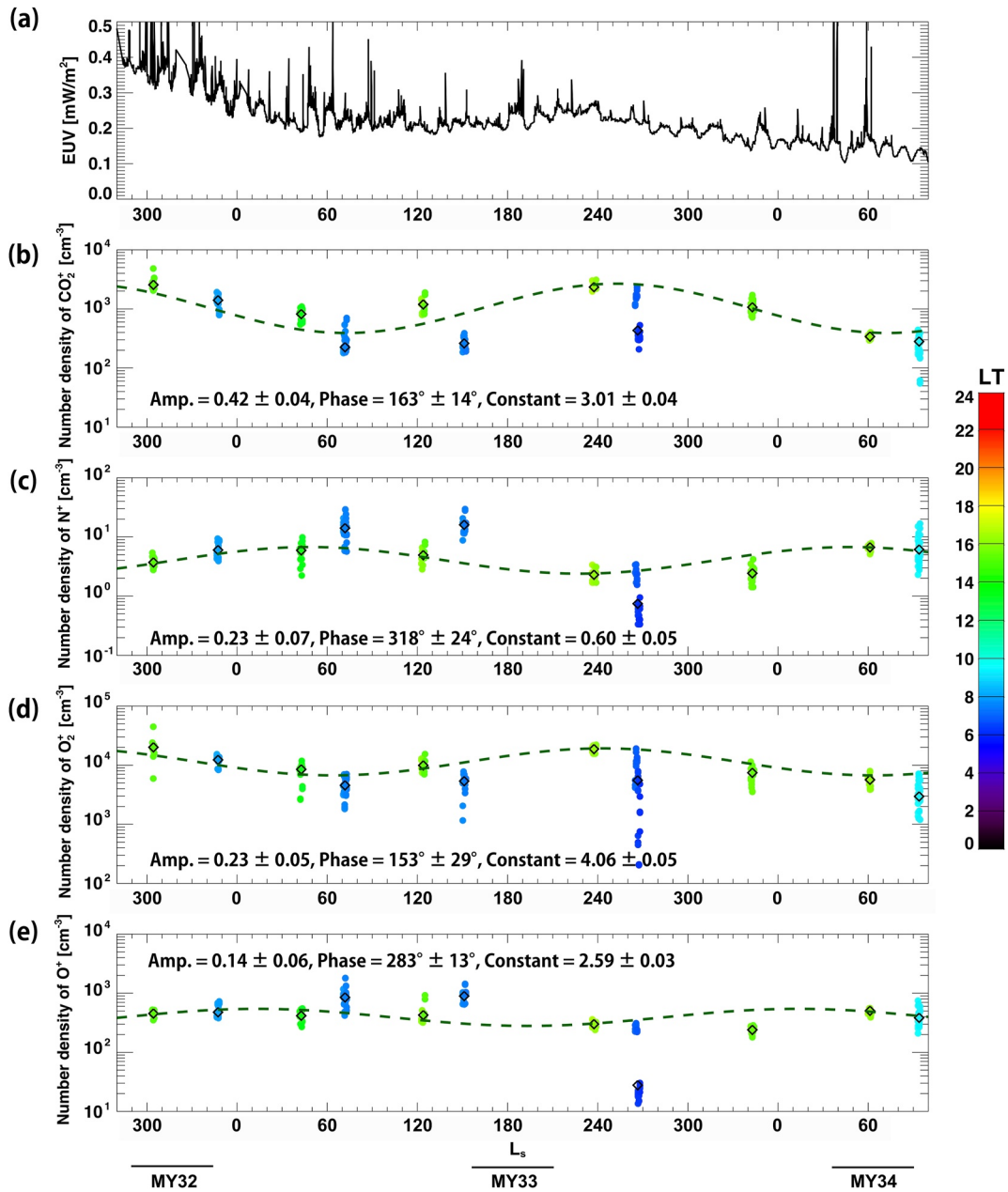

Figure 3. Time variations in ion species and extreme ultra violet irradiance at 17–22 nm as shown in Figure 2. The best fit parameters of the sinusoidal fit are determined in the same way as Figure 2 and are shown in the figures. (b) CO_2^+, (c) N^+, (d) O_2^+, and (e) O^+ number densities.

during L_s = ~320–350 in MY 33 is shown in red, which is discussed in more detail in Section 4.2. Measured densities are binned every 5 km, and median densities are shown as each seasonal profile. The median values of solar EUV irradiance in L_s = 299–310 in MY 32, L_s = 113–133 in MY 33, L_s = 342–346 in MY 33, and L_s = 59–63 in MY 34 are 0.35, 0.19, 0.15, and 0.17 mW/m^2, respectively. The median solar EUV irradiance in L_s = 299–310 in MY 32 is nearly two times larger than that in other seasons.

As observed at a 200 km altitude shown in Figure 2, the vertical profiles of CO_2 and N_2 densities show a seasonal variation in the whole altitude range. A higher density appears in L_s = 299–310, and a lower density appears in L_s = 59–63. CO_2 densities vary significantly compared with other species. Although the O density in L_s = 113–133 shows a relatively lower density than that in L_s = 59–63, it is within the 25% quartiles.

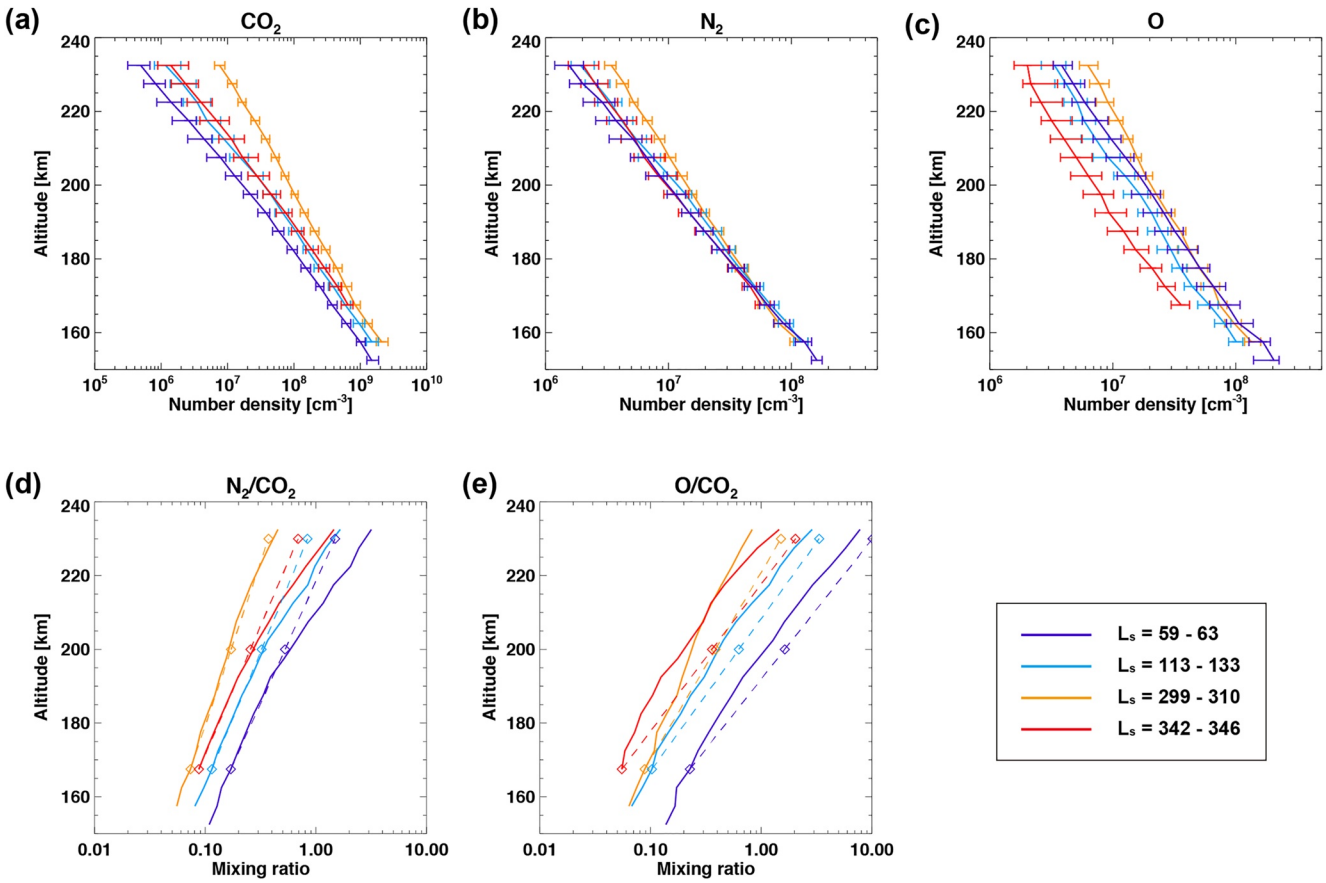

Figure 4. Median vertical profiles of neutral species observed in the northern hemisphere, local time later than 12:00 p.m., and solar zenith angle between 60° and 65°. The line shows median values binned in a 5 km altitude. Horizontal bars show the 25% and 75% quartiles. (a) CO_2, (b) N_2, and (c) O densities. Vertical profiles of atmospheric composition for the same duration are shown in (d) and (e), which are calculated from the median values of (a) to (c). (d) N_2/CO_2 and (e) O/CO_2 ratios. The dashed lines in panels (d) and (e) represent theoretical mixing ratio profiles estimated assuming hydrostatic equilibrium above the homopause. The colors represent the four seasons: L_s = 59–63 (purple), L_s = 113–133 (light blue), L_s = 299–310 (yellow), and L_s = 342–346 (red).

Temperatures in the thermosphere are derived from the scale heights of vertical CO_2 densities between altitudes of 165 and 200 km assuming an isothermal atmosphere. The temperatures derived from each profile at L_s = 59–63, L_s = 113–133, and L_s = 299–310 are 192, 210, and 257 K, respectively. Stone et al. (2018) reported that temperature derived from the Ar scale height is more accurate and higher by 10–20 K than that derived from the CO_2 scale height. When we derive the temperature from the Ar scale heights, the temperatures become 216, 222, and 259 K, respectively. The differences in temperatures between the two are 24, 12, and 2 K, respectively. Derived temperatures are consistent with average temperatures, which vary in association with the solar EUV irradiance, as reported in Bougher et al. (2017). The higher scale height and temperature in L_s = 299–310 is the combination of the effects of both seasonal and solar cycle variations. Therefore, the CO_2 density in the upper atmosphere varies with the solar EUV heating in the thermosphere in addition to the inflation and contraction of the lower atmosphere.

The vertical profiles of N_2/CO_2 and O/CO_2 ratios, shown in Figures 4d and 4e, increase with altitude. In the whole altitude range, a higher mixing ratio appears in L_s = 59–63, and a lower mixing ratio appears in L_s = 299–310. A theoretical vertical structure of the mixing ratio estimated assuming hydrostatic equilibrium above the homopause is written as

$$\frac{n_{z=z'}(A)}{n_{z=z'}(B)} = \frac{n_{z=z_0}(A)}{n_{z=z_0}(B)} \times \exp\left[-(z'-z_0)\left(\frac{1}{H_A}-\frac{1}{H_B}\right)\right] \quad (12)$$

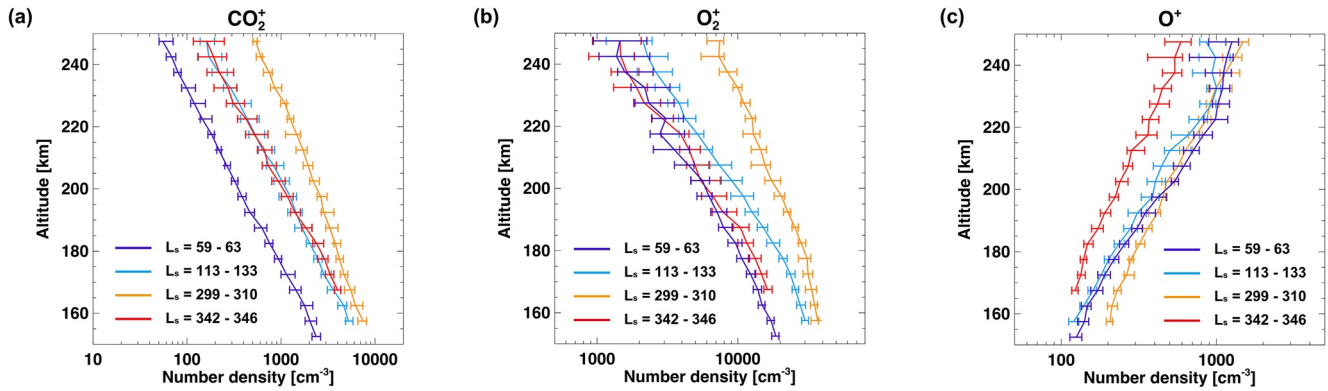

Figure 5. Median vertical profiles of ion species, as shown in Figure 4. (a) CO_2^+, (b) O_2^+, and (c) O^+ densities.

where $n(A)$ is a lighter species, $n(B)$ is a heavier species, and H_A and H_B are the scale heights of A and B (Chassefière & Leblanc, 2004). We defined z_0 as the 167.5 km altitude, and two altitudes were chosen as z': 200.0 and 230.0 km altitude. A is either the N_2 or O density and B is the CO_2 density. The observed N_2/CO_2 and O/CO_2 ratios at 167.5 km and thermospheric temperatures derived from the scale heights of CO_2 densities are substituted. The estimated mixing ratio is shown in Figures 4d and 4e. The observed N_2/CO_2 profiles correspond to the profile estimated assuming hydrostatic equilibrium below a 200 km altitude. Thus, the observed N_2/CO_2 ratio follows diffusive separation below a 200 km altitude. In the case of the O/CO_2 ratio, the observed O/CO_2 ratio is lower than the mixing ratio estimated assuming hydrostatic equilibrium over the whole altitude range. The GCM demonstrates the transport of O from the afternoon to the nightside, and therefore, a lower O/CO_2 ratio appears in the afternoon (Bougher et al., 1990, 2015). The O/CO_2 ratio we observed was measured at approximately 15:00 to 17:00 in LT. The transport of O from the afternoon to the nightside may explain the discrepancy between the observed O/CO_2 ratio and the mixing ratio estimated assuming hydrostatic equilibrium. When we use the temperatures derived from the Ar scale height, the estimated mixing ratios of N_2/CO_2 and O/CO_2 decrease by up to 13% and 24% at a 200 km altitude, respectively, due to the high temperature. However, we confirmed that mixing ratios estimated with the Ar scale height temperature do not affect our result.

Figure 5 shows seasonal variations in median ion densities in vertical profiles between ~150 and ~250 km. Vertical profiles of ion densities are also constrained in the same LT, latitude, and SZA ranges (i.e., the L_s range is the same as for the neutral profiles). A profile in L_s = 342–346 shown in red is discussed in Section 4.2. Vertical structures of ion density also show a clear seasonal variation in the whole altitude range for CO_2^+ and O_2^+. Higher densities appear in L_s = 299–310, and lower densities appear in L_s = 59–63. The scale heights of O_2^+ and CO_2^+ density profiles between altitudes of 180 and 230 km have higher values in L_s = 299–310 than others, which correspond to the higher temperature in the thermosphere during the same period due to the high EUV irradiance. The scale height of the O_2^+ profile is larger than that of the CO_2^+ profile, as expected given their different molecular masses. The O^+ density does not vary significantly with season except during the regional dust event (red). Girazian et al. (2019) showed the O^+ distribution between altitudes of 150 and 400 km shown in Figure 3. The observed O^+ profiles are consistent with those in Figure 3 in Girazian et al. (2019). The differences in CO_2^+, O_2^+, and O^+ number densities between L_s = 59–63 and L_s = 299–310 at a 180 km altitude are by factors of ~5.0, ~2.9, and ~1.3, respectively.

4. Discussion

4.1. Seasonal Variation in Ion Density Under the PCE

In the PCE layer, stationary number densities of CO_2^+, O_2^+, and O^+ are derived such that the photochemical production and loss rates of each ion species are equal. According to the main photochemical reactions in (Equations 1–8), each theoretical ion density can be described by the following equations:

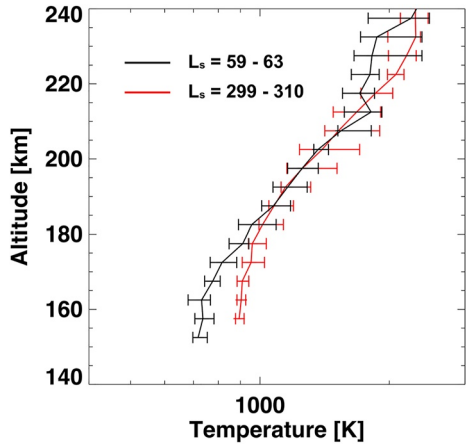

Figure 6. Vertical profiles of median electron temperature observed by the Langmuir Probe and Waves instrument (LPW). Horizontal bars show the 25% and 75% quartiles. The geometry of the LPW is restricted to the same geometry as the NGIMS. Profile measured in L_s = 299–310 is shown in red and that in L_s = 59–63 is in black.

$$\left[CO_2^+\right] = \frac{P\left(CO_2^+\right)}{\left(k_1 + k_3\right)\left[O\right] + k_5\left[e\right]} \tag{13}$$

$$\left[O_2^+\right] = \frac{k_2\left[O^+\right]\left[CO_2\right] + k_3\left[CO_2^+\right]\left[O\right]}{k_4\left[e\right]} \tag{14}$$

$$\left[O^+\right] = \frac{k_1\left[O\right]\left[CO_2^+\right] + P\left(O^+\right)}{k_2\left[CO_2\right]} \tag{15}$$

where k_1, k_2, and k_3 are rate coefficients for reactions (Equations 4–6), respectively. k_4 and k_5 are dissociative recombination rates for CO_2^+ and O_2^+. The rate coefficients for k_4 and k_5 depend on the electron temperature. Since direct photoionization of O_2 is small, we neglected it for the production rates of O_2^+. Thus, we calculated the number densities of ion species and their seasonal variations by Equations 13–15 for L_s = 59–63 (purple profiles in Figures 4 and 5) and L_s = 299–310 (yellow profiles in Figures 4 and 5). The median densities of neutral and ion species shown in Figures 4 and 5 are adopted for the calculation. The electron densities are assumed to be the sum of the O_2^+, CO_2^+, and O^+ densities. Figure 6 represents the vertical profiles of the median electron temperature for the two L_s ranges measured by the LPW. We applied those electron temperature profiles to the estimation of the rate coefficient for k_4 and k_5. In this paper, the photoionization rates of CO_2^+ and O^+ are estimated by the EUVAC solar flux model (Richards et al., 1994). The photoionization rates of O^+ include photoelectron impact ionization. We choose the $F_{10.7}$ flux at Earth as 70 for L_s = 59–63 (i.e., solar minimum condition) and 130 for L_s = 299–310 (i.e., solar mean condition). The seasonal dependence of the photoionization rates is derived from seasonal changes in the Sun-Mars distance.

Ion number densities are estimated below the PCE boundary (altitude of ~200 km). Figure 7 shows estimated ion profiles. The estimated number densities of CO_2^+, O_2^+, and O^+ near 180 km in L_s = 299–310 (L_s = 59–63) are 7.4×10^3 (1.5×10^3), 4.0×10^4 (2.9×10^4), and 1.4×10^2 (98) cm^{-3}, respectively. The densities of CO_2^+, O_2^+, and O^+ near 180 km vary by factors of ~5.1, ~1.4, and ~1.4, respectively. We caution that the absolute number of estimated ion number densities does not correspond with observations. The uncertainty in the rate coefficients might cause those disagreements. However, the uncertainty in the rate coefficients is out of scope because we discuss the relative variations in ion number densities. The PCE model can reproduce the

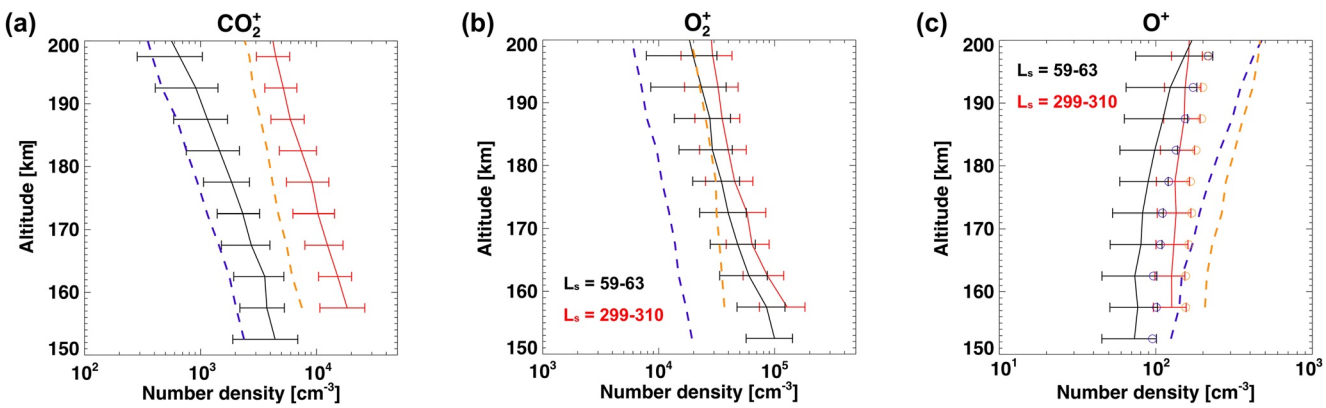

Figure 7. Vertical profiles of estimated number densities under the photochemical equilibrium. The estimation of number density in L_s = 299–310 is shown in red and that in L_s = 59–63 is shown in black. The horizontal bar is the maximum uncertainty based on the deviation between the observed number densities and electron temperature. Dashed lines are the observed median densities shown in Figure 5. The observed number density in L_s = 299–310 is shown in yellow and that in L_s = 59–63 is shown in purple. When we increase the O number densities by a factor of 1.5 based on Fox et al. (2021), the estimated O^+ number density increases (circle in figure c) but is still lower than the observation. Other factors might exist to perfectly reproduce the observed O^+ number density.

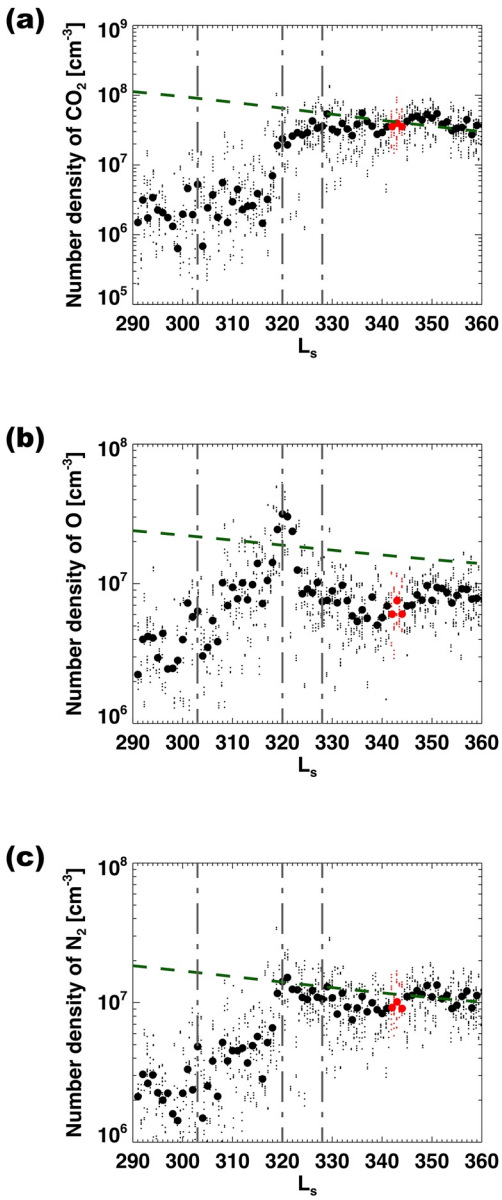

Figure 8. An enlarged view of Figure 2 in CO_2, O, and N_2 densities with all solar zenith angle (SZA) ranges. The scatter is the original number densities observed at altitudes of 199–201 km. The large dots represent the median densities for the same L_s. The red dots represent the SZA range between 60 and 65°. The green dashed line is the sinusoidal curve fit, which corresponds to the seasonal variation in the number density at SZA of 60–65° in the afternoon, which is shown in Figures 2b–2d. The three dashed-dotted lines around L_s of 303°, 320°, and 328° correspond to the peak heating of the atmosphere due to the dust increase in the lower atmosphere described in Liu et al. (2018).

observed variations for CO_2^+ and O^+. However, the variation in O_2^+ density cannot be reproduced. The small variation in O_2^+ density in the PCE model might be the uncertainty in the dissociative recombination rate of k_4 and the effects of dynamics (Fox, 2009). The uncertainty in k_4 might be improved with the new calibrated LPW electron temperature reported in Ergun et al. (2021), however, those data have not been published yet.

As shown in Section 3, the most variable species is CO_2 for neutrals and CO_2^+ for ions. A remarkable variation is found in the term including the CO_2 density and/or that including the CO_2^+ density, and the photoionization rates in Equations 13 and 15. Therefore, it is suggested that the variation in the CO_2 density in the thermosphere and photoionization rate would influence the observed variations in ion densities in the PCE layer.

4.2. Change in Ion Compositions During the Regional Dust Storm Event

The regional dust storm event was found in MY 33 in the range of ~320–350 L_s, which showed the highest infrared absorption at ~0.525 at 610 Pa (Montabone et al., 2015, 2020; see daily column dust optical depth (CDOD) maps by the Mars Climate Database project at http://www-mars.lmd.jussieu.fr/mars/dust_climatology/index.html). Our analysis by NGIMS covers the vertical profiles of neutral and ion species in L_s = 342–346, which are shown as red lines in Figures 4 and 5. Hereafter, we focus on the profiles observed in that period.

In Liu et al. (2018), the increases in neutral CO_2, Ar, N_2, CO, and O densities in response to dust increases in the lower atmosphere during this regional dust event were investigated. However, our observation suggests a decrease in O density. To discuss the differences between Liu et al. (2018) and this study in terms of time variation during the regional dust event, an enlarged view of Figure 2 with all SZA ranges is shown in Figure 8. SZA changes gradually from ~120° to ~40° as L_s changes from 290 to 360. The red dots in Figure 8 represent the SZA range between 60 and 65°. The green dashed line is the sinusoidal fit for SZA of 60–65°, as shown in Figures 2b–2d. Three vertical dashed-dotted lines correspond to the date of peak atmospheric heating due to the dust increase in the lower atmosphere (Liu et al., 2018). As described in Liu et al. (2018), the number of densities in the thermosphere (CO_2, N_2, and O) increase compared to the median densities of the 20° L_s running mean at the peak heating in the lower atmosphere, as shown in Figure 8. On the other hand, our observation focuses on L_s = 342–346 after Liu et al. (2018), which is represented by the red dots. It was found that the CO_2 and N_2 densities agree with the fitting curves of seasonal variation. Meanwhile, the O density is lower than the density of the sinusoidal fit. Our results suggest a decrease in the O density during the regional dust storm. Although the temperature in the lower atmosphere does not have any peak in L_s = 342–346 (Figure 1 in Liu et al., 2018), we must note that dust still exists in the atmosphere (see daily CDOD maps).

As shown in Figures 2 and 4, a vertical profile of CO_2 density in L_s = 342–346 is found within the profiles in L_s = 59–63 to L_s = 299–310. Similarly, a profile of N_2 density in L_s = 342–346 is an intermediate density. Thus, the N_2/CO_2 profile in L_s = 342–346 is within the seasonal variation. The thermospheric temperature derived from the scale height of CO_2 density between altitudes of 165 and 200 km is 202 K, which is an intermediate temperature compared with other seasons. An increase in thermospheric temperature during a regional dust event seems to be insignificant (Keating et al., 1998). The temperatures obtained in this study

are reasonable. The observed N_2/CO_2 profile in L_s = 342–346 follows the diffusive separation corresponding to thermospheric temperatures below a 200 km altitude.

On the other hand, we find that a vertical profile of O density in L_s = 342 – 346 decreases in the whole altitude range between ~165 and ~240 km. The O density at 180 km decreases by ~40% from L_s = 299–310 to L_s = 342–346. We also found decreases in O_2^+ and O^+ in L_s = 342–346 in MY 33. In particular, the vertical profile of O^+ has a lower density than its seasonal variation (i.e., other profiles shown). The O^+ density at 180 km decreases by ~50% from L_s = 299–310 to L_s = 342–346. The O_2^+ density at 180 km decreases by ~40%. Decreases in O and O^+ in the thermosphere and ionosphere during the planet-encircling dust event in 2018 have been found (Elrod et al., 2019; Niu et al., 2021). Our observations showed that regional dust events would also have an impact on the atmospheric composition in the upper atmosphere.

The decrease in O_2^+ and O^+ densities in the PCE layer could be reproduced when the O density decreases in the thermosphere. The decrease in O changes the production rate of O^+ between the O and CO_2^+ reactions (Equation 4). Then, it changes the production rates of O_2^+ between the O^+ and CO_2 reactions (Equation 5), as well as the CO_2^+ and O reactions (Equation 6). The decrease in O observed in this study qualitatively explains the O^+ and O_2^+ densities during the regional dust event.

A change in the dynamic process associated with thermospheric temperature during the dust event would deplete the O density in the afternoon, as simulated in Bougher et al. (1997). To clarify this mechanism, it is necessary to compare observations between the dust storm and non-dust storm conditions using global observational data that cover a wider local time range.

Photochemical reactions with species related to water would also be important for atmospheric composition in the upper atmosphere. During dust events, an enhancement of water vapor in the middle atmosphere has been found (e.g., Aoki et al., 2019; Fedorova et al., 2018; Heavens et al., 2018). The water vapor in the middle atmosphere dissociates, and the mixing ratios of H_2, H, and OH would therefore be enhanced in the thermosphere. The decrease in O may be explained by the reaction between O and OH in the thermosphere. Additionally, H_2 abundances in the thermosphere could affect CO_2^+ and O^+ densities in the ionosphere because H_2 interacts with CO_2^+ and O^+ and then increases the loss rate of CO_2^+ and O^+. It also decreases O_2^+ (Fox, 2015; Krasnopolsky, 2002; Matta et al., 2013). Indeed, an increase in water vapor in the middle atmosphere after the regional dust event in MY 33 was detected by Heavens et al. (2018). This might support the possibility of photochemical reactions in the thermosphere and ionosphere with OH, H_2, and H. Moreover, water group ions (H_2O^+, OH^+, and H_3O^+) and protonated ions have been observed in the Martian ionosphere (Cui et al., 2020; Fox et al., 2015; Niu et al., 2021; Stone et al., 2020). Quantitative estimation including the water group and protonated ions may explain the decrease in O^+ and O_2^+ in more detail.

5. Implication for Heavy Ion Outflow

Hereafter, we show the observed variations in neutral and ion densities in pressure coordinates to discuss the implication for heavy ion outflow and compare our results of O_2^+/O^+ and CO_2^+/O^+ with those of Chaufray et al. (2014). Pressure coordinates are useful for verifying the changes in number densities under the same conditions since they cancel out variations in the inflation and contraction of the lower atmosphere. Figure 9 shows the CO_2 and N_2 number densities as well as CO_2 and O number densities as a function of pressure. CO_2 partial pressure P (Pa) is calculated from the observation assuming the ideal gas law, $P = Nk_bT$, where N is the number density of CO_2 (m^{-3}), k_b is the Boltzmann constant, and T is temperature. Temperatures are derived from the scale heights of CO_2 densities. Around a pressure level of 10^{-7} Pa, the CO_2 and N_2 densities vary by a factor of 1.4 and 2.2, respectively, from L_s = 59–63 to L_s = 299–310, which would be caused by the variation in temperature in the thermosphere. Around the same pressure level, the O density varies by a factor of 2.2 from L_s = 59–63 to L_s = 299–310, which would be explained by the thermospheric temperature and transport of O. It is noted that the O density for L_s = 342–346 shows the lowest density among the profiles. This can be explained by the decrease in the number density during the regional dust event, as discussed above.

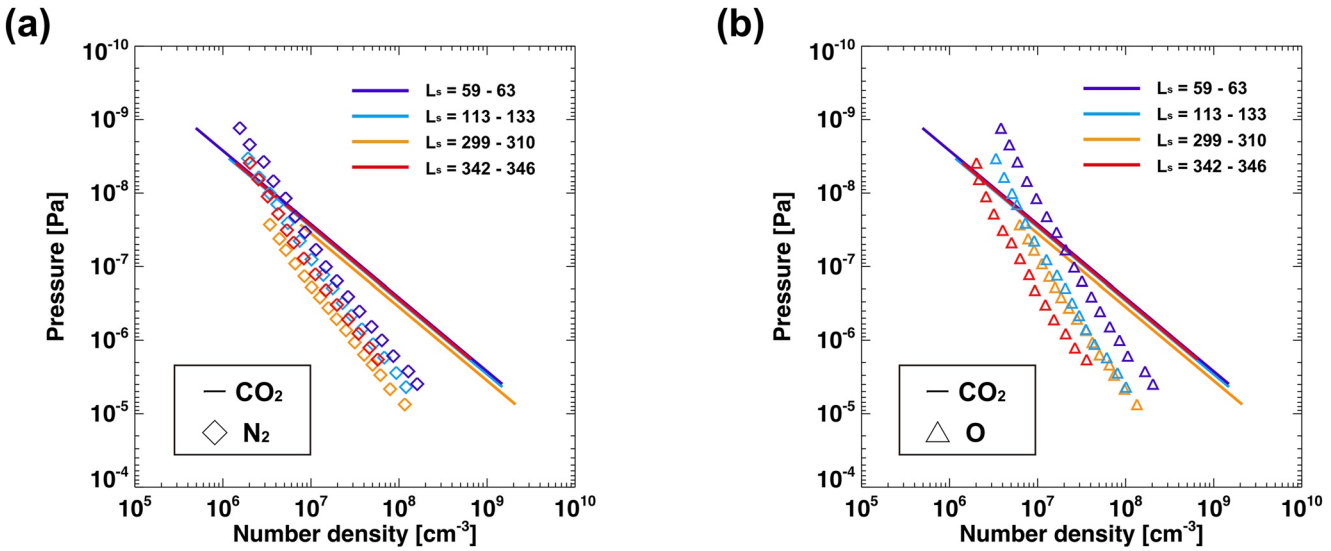

Figure 9. Vertical profiles of neutral species shown in Figure 4 are replaced with pressure coordinates. The pressure level is derived from the CO_2 density and its scale height. The lines are the median CO_2 densities. Diamonds in (a) are the median N_2 densities, and triangles in (b) are the median O densities. Each profile is distinguished by color as in Figure 4.

5.1. Escape Flux

Profiles of ion density are shown in pressure coordinates in Figure 10. Variations in CO_2^+, O_2^+, and O^+ densities are found at each pressure level. Because the ionospheric density follows the PCE, those variations would be influenced by the variation in CO_2, O, and photoionization rates. Additionally, O_2^+ and O^+ densities for L_s = 342–346 are affected by the small O density related to the regional dust event.

The typical neutral exobase is located at a pressure level of ~10^{-7} Pa (cf. Jakosky et al., 2017). Our observation shows that the number densities of CO_2^+, O_2^+, and O^+ vary above the exobase by factors of 2.9, 2.3, and 2.3, respectively, based on the difference between L_s = 59–63 and L_s = 299–310 for CO_2^+ and between L_s = 342–346 and L_s = 299–310 for O_2^+ and O^+. This variation would in turn modify the escape rate of ionospheric ion outflow (e.g., Carlsson et al., 2006; Fox, 1997; Lundin et al., 2004) if it is assumed that ionospheric ion outflow occurs above the neutral exobase. An increase in low-energy O_2^+ and O^+ escape fluxes with solar EUV flux is observed by ASPERA-3 aboard Mars Express as well as the ion sensor Suprathermal And Thermal Ion Composition aboard MAVEN (Dong et al., 2017; Dubinin, Fraenz, Pätzold, Andrews, et al., 2017; Dubinin, Fraenz, Pätzold, McFadden, et al., 2017). In our observations, the highest number densities of major ions appear in L_s = 299–310 in MY 32 when the solar EUV irradiance is higher than for other seasons. It must be emphasized that not only the change in ionization rates but also the compositional

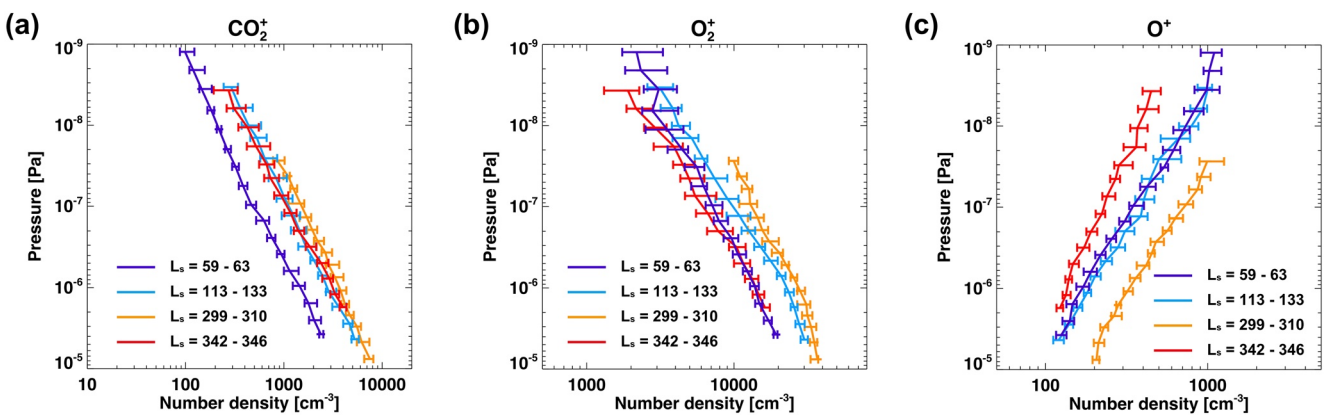

Figure 10. Vertical profiles of ion species shown in Figure 5 are replaced with neutral pressure coordinates.

Table 1
Relative Seasonal Variations in the O_2^+/O^+ and CO_2^+/O^+ Density Ratios Compared to Those Observed in L_s = 59–63

	L_s = 59–63	L_s = 113–133	L_s = 299–310	L_s = 342–346
O_2^+/O^+	1.00 ± 0.34	1.09 ± 0.34	0.85 ± 0.22	1.11 ± 0.58
CO_2^+/O^+	1.00 ± 0.28	1.88 ± 0.68	1.49 ± 0.52	2.92 ± 0.91

Note. As a typical value, density ratios around a pressure level of 8×10^{-8} Pa are shown. Uncertainties in the ion density ratios are maximum errors. The largest value of the quartile around a pressure level of 8×10^{-8} Pa is assumed to be the deviation of the number density.

variation in the neutral atmosphere is suggested to be important to determine the ionospheric densities from the present study. Martian ion outflow is also affected by the solar wind, the direction of the motional electric field (Dubinin, Fraenz, Pätzold, McFadden, et al., 2017; Dubinin et al., 2018; Lundin et al., 2008), and the crustal magnetic fields in the southern hemisphere (Dong et al., 2015).

5.2. Mass Composition of the Escaping Ion

According to the GCM results in Chaufray et al. (2014), the dayside density ratios of O_2^+/O^+ and CO_2^+/O^+ can seasonally vary by up to one order of magnitude at a pressure level of 8×10^{-8} Pa. Larger density ratios are predicted during the solstice season. The variability of the density ratio simulated by Chaufray et al. (2014) is explained by the variation in neutral compositions of CO_2 and O due to the variability of the homopause position (González-Galindo et al., 2009). In their neutral atmospheric model, the pressure level of the homopause altitude can vary by up to one order of magnitude due to strengthened global circulation during the solstice season (González-Galindo et al., 2009). On the other hand, we did not obtain such a significant variation in the O_2^+/O^+ and CO_2^+/O^+ ratios around a pressure level of 8×10^{-8} Pa. As summarized in Table 1, the relative variations in O_2^+/O^+ and CO_2^+/O^+ ratios are calculated, and each ratio is normalized by the value for L_s = 59–63. As we can see, the O_2^+/O^+ and CO_2^+/O^+ ratios vary by factors of ∼1.3 and ∼3.0, respectively. However, the variation in the O_2^+/O^+ ratio is smaller than the uncertainties. The observed variabilities in the ion composition suggest that the effects of changes in homopause altitude on neutral and ion compositions at a certain pressure are not as obvious as the results in Chaufray et al. (2014). According to Yoshida et al. (2020), the dayside homopause altitude is suggested to be located around a certain pressure level. The homopause pressure level can be estimated by extrapolating the N_2/CO_2 profile and finding the pressure level where the N_2/CO_2 ratio is equal to the lower atmospheric ratio (cf. Slipski et al., 2018; Trainer et al., 2019). The averaged homopause level in this study is located at approximately 5.25×10^{-5} Pa, and the variability is only a factor of 4.

Recently, the seasonal variation in the O/CO_2 profile in the thermosphere has been improved more realistically in the Mars Climate Database (MCD) model (Millour et al., 2018). The O/CO_2 ratio at a certain pressure is less variable than that shown in González-Galindo et al. (2009). Thus, simulated O_2^+/O^+ and CO_2^+/O^+ density ratios based on the MCD would be improved, and such large variations suggested in Chaufray et al. (2014) would not be obtained.

A several-fold change in the CO_2^+/O^+ ratio is observed over the entire pressure level range. It also suggests that the ratio of CO_2^+/O^+ escape (e.g., Carlsson et al., 2006; Inui et al., 2018, 2019) can vary several-fold due to seasonal and dust storm variations.

6. Conclusions

We present the variations in neutral and ion densities in the upper atmosphere observed by MAVEN/NGIMS to clarify (a) the vertical coupling between the lower thermosphere and upper neutral atmosphere and (b) the coupling between the ionosphere and thermosphere and then to discuss the effects on heavy ion outflow.

The thermospheric densities of CO_2, N_2, and O show seasonal sinusoidal variations at a 200 km altitude, with higher densities around perihelion and lower densities around aphelion. The most variable species is CO_2, which causes variations in the N_2/CO_2 and O/CO_2 in the upper thermosphere. The variability in number densities and mixing ratios at a 200 km altitude resembles the variations in CO_2, N_2, and N_2/CO_2 in the lower thermosphere reported by Yoshida et al. (2020). This suggests that densities in the upper thermosphere change in response to the variation in the lower thermosphere. In the ionosphere, seasonal sinusoidal variation is found in the CO_2^+ and O_2^+ number densities at a 200 km altitude, corresponding to the seasonal trend of neutral CO_2 in the upper thermosphere. However, that of the O^+ density is less discernible. The N^+ number density shows the opposite seasonal variation as that of the CO_2^+ number density. This can be explained by the process of N^+ loss, which is destroyed by reactions with CO_2 below its peak altitude

(normally ~220 km under solar minimum conditions; Fox et al., 1996). The three-fold seasonal variation in CO_2 compared to N_2 would enhance the process of N^+ loss and decrease the N^+ density, as observed.

The vertical structures between altitudes of ~150 and ~250 km for neutral and ion densities show variations due to the season and solar activity. The observed CO_2^+, O_2^+, and O^+ densities at a 180 km altitude vary by factors of ~5.0, ~2.9, and ~1.3, respectively. We estimated the variation in ion densities using a PCE model below a ~200 km altitude. The observed variations in ion number densities due to the combination of seasonal and solar cycle variations are reproduced by the model except for O_2^+.

In addition, decreases in the number densities of O, O_2^+, and O^+ between altitudes of ~165 and ~250 km are found for L_s = 342–346 in MY 33 during the regional dust event. Since the photochemistry of O_2^+ is controlled by the reactions between O^+ and CO_2 as well as between CO_2^+ and O and that of O^+ is controlled by the reaction between O and CO_2^+, a significant decrease in O density would qualitatively lead to a decrease in O^+ and O_2^+ density. Different behavior of ionospheric compositions during the dust event is suggested.

The vertical structures of neutral and ion number densities in pressure coordinates are shown to discuss the effects on heavy ion outflow. The number density of ion species varies several-fold. The change in ion density at a certain pressure level in the ionosphere can modify the ionospheric ion outflow. In the case of ionospheric composition, we observed that the O_2^+/O^+ and CO_2^+/O^+ vary by factors of ~1.3 and ~3.0, respectively, around a pressure level of 8×10^{-8} Pa. Chaufray et al. (2014) simulated an enhancement of one order of magnitude in those density ratios during the solstice season. The observed variations in ionospheric composition at a certain pressure level suggest that the effects of the variation in the dayside homopause altitude on the ionospheric composition are smaller than those predicted in the model. The clear variations in the CO_2^+/O^+ ratio would also suggest that the composition of the ionospheric ion outflow can vary several-fold due to the combination of seasonal and dust-related variations.

In the present study, we only focus on the coupling between the ionosphere and the thermosphere. The simultaneous observation of ion outflow and ionospheric density would provide further suggestions about the connection between the reservoir region and ion outflow.

Data Availability Statement

The MAVEN/NGIMS level 2 version 8 revision 1 data set used in this study is available at the NASA PDS at https://pds-atmospheres.nmsu.edu/data_and_services/atmospheres_data/MAVEN/ngims.html. The MAVEN/LPW level 2 version 3 data set are also available at the NASA PDS at https://pds-ppi.igpp.ucla.edu/search/?sc=MAVEN&t=Mars&i=LPW. Bundle LID is urn:nasa:pds:maven.lpw.derived:data.lp.nt. MAVEN/EUVM level 2 version 11 revision 4 data are available through the NASA PDS at https://pds-ppi.igpp.ucla.edu/search/?sc=MAVEN&t=Mars&i=EUV. The data set used in this study are available at Yoshida et al. (2021), Data set of MAVEN/NGIMS density and estimated ion number densities under the photochemical equilibrium, Zenodo (https://doi.org/10.5281/zenodo.5115241).

Acknowledgments
The MAVEN project is supported by NASA through the Mars Exploration program. This study was supported by Grant-in-Aids for Scientific Research (C) No. 19K03943, Scientific Research (A) No. 19H00707, (A) No. 20H00192, and Grant-in-Aid for Scientific Research on Innovative Areas for 20H0460 from JSPS. This work was supported by JSPS KAKENHI Grant Number JP18H05439, JP18KK0093, and NINS Astrobiology Center satellite research. This work was conducted under NASA's MAVEN participating Scientist Program (proposal #12-MAVENPS12-0017, PI: K. Seki). N. Yoshida is supported by the Japanese Society for the Promotion of Science (JP21J13710) and the international joint Graduate Program in Earth and Environmental Sciences, Tohoku University (GP-EES). N. Yoshida appreciates constructive comments and feedback from anonymous reviewers.

References

Andersson, L., Ergun, R. E., Delory, G. T., Eriksson, A., Westfall, J., Reed, H., et al. (2015). The Langmuir Probe and Waves (LPW) instrument for MAVEN. *Space Science Reviews*, *195*, 173–198. https://doi.org/10.1007/s11214-015-0194-3

Aoki, S., Vandale, A. C., Daerden, F., Villanueva, G. L., Liuzzi, G., Thomas, I. R., et al. (2019). Water vapor vertical profiles on Mars in dust storms observed by TGO/NOMAD. *Journal of Geophysical Research: Planets*, *124*, 3482–3497. https://doi.org/10.1029/2019JE006109

Benna, M., Mahaffy, P. R., Grebowsky, M., Fox, J. L., Yelle, R. V., & Jakosky, B. M. (2015). First measurement of composition and dynamics of the Martian ionosphere by MAVEN's neutral gas and ion mass spectrometer. *Geophysical Research Letters*, *42*, 8958–8965. https://doi.org/10.1002/2015GL066146

Bougher, S. W., Engel, S., Roble, R. G., & Foster, B. (1999). Comparative terrestrial planet thermospheres 2. Solar cycle variation of global structure and winds at equinox. *Journal of Geophysical Research*, *104*(E7), 16591–16611.

Bougher, S. W., Murphy, J., & Haberle, R. M. (1997). Dust storm impacts on the Mars upper atmosphere. *Advances in Space Research*, *19*(8), 1255–1260.

Bougher, S. W., Pawlowski, D., Bell, J. M., Nelli, S., McDunn, T., Murphy, J. R., et al. (2015). Mars Global Ionosphere-Thermosphere Model (MGITM): Solar cycle, seasonal, and diurnal variations of the Mars upper atmosphere. *Journal of Geophysical Research: Planets*, *120*, 311–342. https://doi.org/10.1002/2014JE004715

Bougher, S. W., Roble, R. G., Ridley, E. C., & Dickinson, R. E. (1990). The Mars thermosphere 2. General circulation with coupled dynamics and composition. *Journal of Geophysical Research*, *95*(B9), 14811–14827.

Bougher, S. W., Roeten, K. J., Olsen, K., Mahaffy, P. R., Benna, M., Elrod, M., et al. (2017). The structure and variability of Mars dayside thermosphere from MAVEN NGIMS and IUVS measurements: Seasonal and solar activity trends in scale heights and temperature. *Journal of Geophysical Research: Space Physics*, *122*, 1296–1313. https://doi.org/10.1029/1998je001019

Carlsson, E., Fedorov, A., Baradash, S., Budnik, E., Grigoriev, A., Gunell, H., et al. (2006). Mass composition of the escaping plasma at Mars. *Icarus*, *182*, 320–328. https://doi.org/10.1016/j.icarus.2005.09.020

Chassefière, E., & Leblanc, F. (2004). Mars atmospheric escape and evolution; interaction with the solar wind. *Planetary and Space Science*, *52*, 1039–1058. https://doi.org/10.1016/j.pss.2004.07.002

Chaufray, J.-Y., González-Galindo, F., Forget, F., Lopez-Valverde, M., Leblanc, F., Modolo, R., et al. (2014). Three-dimensional Martian ionosphere model: II. Effect of transport process due to pressure gradients. *Journal of Geophysical Research: Planets*, *119*, 1614–1636. https://doi.org/10.1002/2013JE004551

Cui, J., Ren, Z.-P., Wu, Z.-P., Wu, X.-S., Hao, Y.-Q., & Wei, Y. (2020). Abnormal dawn-dusk asymmetry of protonated ions in the Martian ionosphere. *The Astrophysical Journal Letters*, *895*, L43. https://doi.org/10.3867/2041-8213/ab930c

Dong, C., Bougher, S. W., Ma, Y., Toth, G., Lee, Y., Nagy, A. F., et al. (2015). Solar wind interaction with the Martian upper atmosphere: Crustal field orientation, solar cycle, and seasonal variations. *Journal of Geophysical Research: Space Physics*, *120*, 7857–7872. https://doi.org/10.1002/2015JA020990

Dong, Y., Fang, X., Brain, D. A., McFadden, J. P., Halekas, J. S., Connerney, J. E. P., et al. (2017). Seasonal variability of Martian ion escape through the plume and tail from MAVEN observations. *Journal of Geophysical Research: Space Physics*, *122*, 4009–4022. https://doi.org/10.3847/2041-8213/ab930c

Dubinin, E., Fraenz, M., Pätzold, M., Andrews, D., Vaisberg, O., Zelenyi, L., & Barabash, S. (2017). Martian ionosphere observed by Mars Express. 2. Influence of solar irradiance on upper ionosphere and escape fluxes. *Planetary and Space Science*, *145*, 1–8. https://doi.org/10.1016/j.pss.2017.07.022

Dubinin, E., Fraenz, M., Pätzold, M., McFadden, J., Halekas, J. S., Connerney, J. E. P., et al. (2018). Martian ionosphere observed by MAVEN. 3. Influence of solar wind and IMF on upper ionosphere. *Planetary and Space Science*, *160*, 56–65. https://doi.org/10.1016/j.pss.2018.03.016

Dubinin, E., Fraenz, M., Pätzold, M., McFadden, J., Mahaffy, P. R., Eparvier, F., et al. (2017). Effects of solar irradiance on the upper ionosphere and oxygen ion escape at Mars: MAVEN observations. *Journal of Geophysical Research: Space Physics*, *122*, 7142–7152. https://doi.org/10.1016/j.pss.2017.07.002

Elrod, M. K., Bougher, S. W., Roeten, K., Sharrar, R., & Murphy, J. (2019). Structural and compositional changes in the upper atmosphere related to the PEDE-2018 dust event on Mars as observed by MAVEN NGIMS. *Geophysical Research Letters*, *47*. https://doi.org/10.1029/2019GL084378

Eparvier, F. G., Chamberlin, P. C., Woods, T. N., & Thiemann, E. M. B. (2015). The solar extreme ultraviolet monitor for MAVEN. *Space Science Reviews*, *195*, 293–301. https://doi.org/10.1007/s11214-015-0195-2

Ergun, R. E., Andersson, L. A., Fowler, C. M., Thaller, S. A., & Yelle, R. V. (2021). In-situ measurements of electron temperature and density in Mars' dayside ionosphere. *Geophysical Research Letters*, *48*. https://doi.org/10.1029/2021GL093623

Ergun, R. E., Morooka, M. W., Andersson, L. A., Fowler, C. M., Delory, G. T., Andrews, D. J., et al. (2015). Dayside electron temperature and density profiles at Mars: First results from the MAVEN Langmuir probe and waves instrument. *Geophysical Research Letters*, *42*, 8846–8853. https://doi.org/10.1002/2015GL065280

Fang, X., Ma, Y., Lee, Y., Bougher, S., Liu, G., Benna, M., et al. (2020). Mars dust storm effects in the ionosphere and magnetosphere and implications for atmospheric carbon loss. *Journal of Geophysical Research: Space Physics*, *125*, e2019JA026838. https://doi.org/10.1029/2019JA026838

Fedorova, A., Bertaux, J.-L., Betsis, D., Montmessin, F., Korablev, O., Maltagliati, L., & Clarke, J. (2018). Water vapor in the middle atmosphere of Mars during the 2007 global dust storm. *Icarus*, *300*, 440–457. https://doi.org/10.1029/2019ja026838

Forget, F., Montmessin, F., Bertaux, J.-L., González-Galindo, F., Lebonnois, S., Quémerais, E., et al. (2009). Density and temperatures of the upper Martian atmosphere measured by stellar occultations with Mars Express SPICAM. *Journal of Geophysical Research*, *114*, E01004. https://doi.org/10.1029/2008JE003086

Fox, J. L. (1997). Upper limits to the outflow of ions at Mars: Implications for atmospheric evolution. *Geophysical Research Letters*, *24*(22), 2901–2904.

Fox, J. L. (2009). Morphology of the dayside ionosphere of Mars: Implications for ion outflows. *Journal of Geophysical Research*, *114*, E12005. https://doi.org/10.1029/97gl52842

Fox, J. L. (2015). The chemistry of protonated species in the Martian ionosphere. *Icarus*, *252*, 366–392. https://doi.org/10.1016/j.icarus.2015.01.010

Fox, J. L., Benna, M., Mahaffy, P. R., & Jakosky, B. M. (2015). Water and water ions in the Martian thermosphere/ionosphere. *Geophysical Research Letters*, *42*, 8977–8985. https://doi.org/10.1002/2015GL065465

Fox, J. L., Benna, M., McFadden, J. P., Jakosky, B. M., the MAVEN NGIMS team, & the MAVEN LPW team. (2021). Rate coefficients for the reactions of CO_2^+ with O: Lessons from MAVEN at Mars. *Icarus*, *358*, 114186. https://doi.org/10.1016/j.icarus.2020.114186

Fox, J. L., Johnson, A. S., Ard, S. G., Shuman, N. S., & Viggiano, A. A. (2017). Photochemical determination of O densities in the Martian thermosphere: Effect of a revised rate coefficient. *Geophysical Research Letters*, *44*, 8099–8106. https://doi.org/10.1002/2017GL074562

Fox, J. L., & Sung, K. Y. (2001). Solar activity variations of the Venus thermosphere/ionosphere. *Journal of Geophysical Research*, *106*(A10), 21305–21335. https://doi.org/10.1029/2001JA000069

Fox, J. L., Zhou, P., & Bougher, S. W. (1996). The Martian thermosphere/ionosphere at high and low solar activities. *Advances in Space Research*, *17*(11), 203–218.

Girazian, Z., Mahaffy, P., Lee, Y., & Thiemann, E. M. B. (2019). Seasonal, solar zenith angle, and solar flux variations of O^+ in the topside ionosphere of Mars. *Journal of Geophysical Research: Space Physics*, *124*. https://doi.org/10.1029/2018JA026086

González-Galindo, F., Forget, F., López-Valverde, M. A., Angelats i Coll, M., & Millour, E. (2009). A ground-toexosphere Martian general circulation model: 1. Seasonal, diurnal, and solar cycle variation of thermosphere temperatures. *Journal of Geophysical Research*, *114*, E04001. https://doi.org/10.1029/2008JE003246

Gröller, H., Montmessin, F., Yelle, R. V., Lefèvre, F., Forget, F., Schneider, N. M., et al. (2018). MAVEN/IUVS stellar occultation measurements of Mars atmospheric structure and composition. *Journal of Geophysical Research: Planets*, *123*, 1449–1483. https://doi.org/10.1029/2017JE005466

Gupta, N., Venkateswara, R., & Kadhane, U. R. (2019). Dawn-dusk asymmetries in the Martian upper atmosphere. *Journal of Geophysical Research: Planets*, *124*, 3219–3230. https://doi.org/10.1029/2019JE006151

Heavens, N. G., Kleinböhl, A., Chaffin, M. S., Halekas, J. S., Kass, D. M., Hayne, P. O., et al. (2018). Hydrogen escape from Mars enhanced by deep convection in dust storms. *Nature Astronomy*, *2*, 126–132. https://doi.org/10.1038/s41550-017-0353-4

Inui, S., Seki, K., Namekawa, T., Sakai, S., Brain, D. A., Hara, T., et al. (2018). Cold dense ion outflow observed in the Martian-induced magnetotail by MAVEN. *Geophysical Research Letters*, *45*, 5283–5289. https://doi.org/10.1029/2018GL077584

Inui, S., Seki, K., Sakai, S., Brain, D. A., Hara, T., McFadden, J. P., et al. (2019). Statistical study of heavy ion outflows from Mars observed in the Martian-induced magnetotail by MAVEN. *Journal of Geophysical Research: Space Physics*, *124*, 5482–5497. https://doi.org/10.1029/2018JA026452

Jakosky, B. M., Slipski, M., Benna, M., Mahaffy, P., Elrod, M., Yelle, R., et al. (2017). Mar's atmospheric history derived from upper-atmosphere measurements of $^{38}Ar/^{36}Ar$. *Science*, *355*(6332), 1408–1410. https://doi.org/10.1126/science.aai7721

Keating, G. M., Bougher, S. W., Zurek, R. W., Tolson, R. H., Cancro, G. J., Noll, S. N., et al. (1998). The structure of the upper atmosphere of Mars: In situ accelerometer measurements from Mars Global Surveyor. *Science*, *279*(5357), 1672–1676. https://doi.org/10.1126/science.279.5357.1672

Krasnopolsky, V. A. (2002). Mars' upper atmosphere and inosphere at low, median, and high solar activities: Implications for evolution of water. *Journal of Geophysical Research*, *107*. https://doi.org/10.1029/2001JE001809

Liu, G., England, S. L., Lillis, R. J., Withers, P., Mahaffy, P. R., Rowland, D. E., et al. (2018). Thermospheric expansion associated with dust increase in the lower atmosphere on Mars observed by MAVEN/NGIMS. *Geophysical Research Letters*, *45*, 2901–2910. https://doi.org/10.1002/2018GL077525

Lundin, R., Barabash, S., Andersson, H., Holmström, M., Grigoriev, A., Yamauchi, M., et al. (2004). Solar wind-induced atmospheric erosion at Mars: First results from ASPERA-3 on Mars Express. *Science*, *305*(5692), 1933–1936. https://doi.org/10.1126/science.1101860

Lundin, R., Barabash, S., Fedorov, A., Holmström, M., Nilsson, H., Sauvaud, J.-A., & Yamauchi, M. (2008). Solar forcing and planetary ion escape from Mars. *Geophysical Research Letters*, *35*, L09203. https://doi.org/10.1029/2007GL032884

Lundin, R., Barabash, S., Holmstöm, M., Nilsson, H., Yamauchi, M., Dubinin, E. M., & Fraenz, M. (2009). Atmospheric origin of cold ion escape from Mars. *Geophysical Research Letters*, *36*, L17202. https://doi.org/10.1029/2009GL039341

Lundin, R., Lammer, H., & Ribas, I. (2007). Planetary magnetic fields and solar forcing: Implications for atmospheric evolution. *Space Science Reviews*, *129*, 245–278. https://doi.org/10.1007/s11214-007-9176-4

Mahaffy, P. R., Benna, M., Elrod, M., Yelle, R. V., Bougher, S. W., Stone, S. W., & Jakosky, B. M. (2015). Structure and composition of the neutral upper atmosphere of Mars from the MAVEN NGIMS investigation. *Geophysical Research Letters*, *42*, 8951–8957. https://doi.org/10.1002/2015GL065329

Mahaffy, P. R., Benna, M., King, T., Harpold, D. N., Arvey, R., Barciniak, M., et al. (2014). The neutral gas an ion mass spectrometer on the Mars atmosphere and volatile evolution mission. *Space Science Reviews*, *195*, 49–73. https://doi.org/10.1007/s11214-014-0091-1

Matta, M., Withers, P., & Mendillo, M. (2013). The composition of Mars' topside ionosphere: Effects of hydrogen. *Journal of Geophysical Research: Space Physics*, *118*, 2681–2693. https://doi.org/10.1002/jgra.50104

Millour, E., Forget, F., Spiga, A., Vals, M., & Zakharov, V. (2018). *The Mars Climate Database (version 5.3). Scientific Workshop "from Mars Express to ExoMars"*. ESAC.

Montabone, L., Forget, F., Millour, E., Wilson, R. J., Lewis, S. R., Cantor, B., et al. (2015). Eight-year climatology of dust optical depth on Mars. *Icarus*, *251*, 65–95. https://doi.org/10.1016/j.icarus.2014.12.034

Montabone, L., Spiga, A., Kass, D. M., Kleinböhl, A., Forget, F., & Millour, E. (2020). Martian year 34 column dust climatology from mars climate sounder observations: Reconstructed maps and model simulations. *Journal of Geophysical Research: Planets*, *125*, e2019JE006111. https://doi.org/10.1029/2019JE006111

Niu, D.-D., Cui, J., Wu, S.-Q., Gu, H., Cao, Y.-T., Wu, Z.-P., et al. (2021). Species-Dependent response of the Martian ionosphere to the 2018 global dust event. *Journal of Geophysical Research: Planets*, *126*. https://doi.org/10.1029/2020JE006679

Richards, P. G., Fennelly, J. A., & Torr, D. G. (1994). EUVAC: A solar EUV flux model for aeronomic calculations. *Journal of Geophysical Research*, *99*(A5), 8981–8992. https://doi.org/10.1029/94JA00518

Schunk, R. W., & Nagy, A. F. (2009). *Ionospheres, 2nded*. Cambridge University Press.

Slipski, M., Jakosky, B. M., Benna, M., Elrod, M., Mahaffy, P., Kass, D., et al. (2018). Variability of Martian turbopause altitudes. *Journal of Geophysical Research: Planets*, *123*, 2939–2957. https://doi.org/10.1029/2018JE005704

Stone, W. S., Yelle, R. V., Benna, M., Elrod, M. K., & Mahaffy, P. R. (2018). Thermal structure of the Martian upper atmosphere from MAVEN NGIMS. *Journal pf Geophysical Research: Planets*, *123*, 2842–2867. https://doi.org/10.1029/2018JE005559

Stone, W. S., Yelle, R. V., Benna, M., Lo, D. Y., Elrod, M. K., & Mahaffy, P. R. (2020). Hydrogen escape from Mats is driven by seasonal and dust storm transport of water. *Science*, *370*(6518), 824–831. https://doi.org/10.1126/science.aba5229

Thiemann, E. M. B., Eparvier, F. G., Bougher, S. W., Dominique, M., Andersson, L., Girazian, Z., et al. (2018). Mars thermospheric variability revealed by MAVEN EUVM solar occultations: Structure at aphelion and perihelion and response to EUV forcing. *Journal of Geophysical Research: Planets*, *123*, 2248–2269. https://doi.org/10.1029/2018JE005550

Trainer, M. G., Wong, M. H., McConnochie, T. H., Franz, H. B., Atreya, S. K., Conrad, P. G., et al. (2019). Seasonal variations in atmospheric composition as measured in Gale crater, Mars. *Journal of Geophysical Research - B: Solid Earth and Planets*, *124*, 3000–3024. https://doi.org/10.1029/2019JE006175

Withers, P. (2009). A review of observed variability in the dayside ionosphere of Mars. *Advances in Space Research*, *44*, 277–307. https://doi.org/10.1016/j.asr.2009.04.027

Withers, P., Flynn, C. L., Vogt, M. F., Mayyasi, M., Mahaffy, P., Benna, M., et al. (2019). Mar's dayside upper ionospheric composition is affected by magnetic field conditions. *Journal of Geophysical Research: Space Physics*, *124*, 3100–3109. https://doi.org/10.1029/2018JA026266

Withers, P., & Pratt, R. (2013). An observational study of the response of the upper atmosphere of Mars to lower atmospheric dust storms. *Icarus*, *225*, 378–389. https://doi.org/10.1016/j.icarus.2013.02.032

Withers, P., Vogt, M., Mahaffy, P., Benna, M., Elrod, M., & Jakosky, B. (2015). Changes in the thermosphere and ionosphere of Mars from Viking to MAVEN. *Geophysical Research Letters*, *42*, 9071–9079. https://doi.org/10.1002/2015GL065985

Yoshida, N., Nakagawa, H., Terada, N., Evans, J. S., Schneider, N. M., Jain, S. K., et al. (2020). Seasonal and latitudinal variations of dayside N_2/CO_2 ratio in the Martian thermosphere derived from MAVEN IUVS observations. *Journal of Geophysical Research: Planets*, *125*, e2020JE006378. https://doi.org/10.1029/2020JE006378

Yoshida, N., Terada, N., Nakagawa, H., Brain, D. A., Sakai, S., Nakamura, Y., et al. (2021). Dataset of MAVEN/NGIMS density and estimated ion number densities under the photochemical equilibrium (Version 1). *Zenodo*. https://doi.org/10.5281/zenodo.5115241